Supplementary Information

Both sub-ambient and above-ambient conditions: a comprehensive approach for efficient use of radiative cooling

Huajie Tang[a], Chenyue Guo[a], Fan Fan[a], Haodan Pan[a], Qihao Xu[a], Dongliang Zhao[a,b,c,]*

a. *School of Energy and Environment, Southeast University, Nanjing 210096, China.*

b. *Institute of Science and Technology for Carbon Neutrality, Southeast University, Nanjing 210096, China*

c. *Engineering Research Center of Building Equipment, Energy, and Environment, Ministry of Education, Nanjing 210096, China*

*Corresponding author's e-mail: *dongliang_zhao@seu.edu.cn*

TABLE OF CONTENTS

Section 1: The concept of circuit self-switching

The mechanisms of electric current and heat flow are highly analogous. For electrical current transport, the ability of electrons to migrate is determined by the material's conductivity (conductor, semiconductor, insulator), and the direction of current flow is determined by the voltage difference. In the case of radiative heat transfer, the ability of heat to propagate is determined by the material's emissivity (black body, gray body, white body), and the direction of heat transfer is determined by the temperature gradient. How can energy transfer be spontaneously initiated and terminated based on the potential difference across the two ends? In the field of electronics, metal-oxide-semiconductor field-effect transistors (MOSFETs) (the red symbol in Fig. s1) are designed to self-switch the electric circuit, by inducing the flow of electrons in semiconductors through directional changes in voltage.

Specifically, MOSFETs contains three electrodes. The electrode 'D' and 'S' are N-type hybrid semiconductors, and the electrode 'G' is a P-type hybrid semiconductor coated with a metal-oxide layer. So that if the electrode 'G' contacts with positive voltage, the circuit will connect.

Here, we designed the ISRC to achieve the self-switching of the thermal radiation by inducing step changes in emissivity through directional variations in temperature.

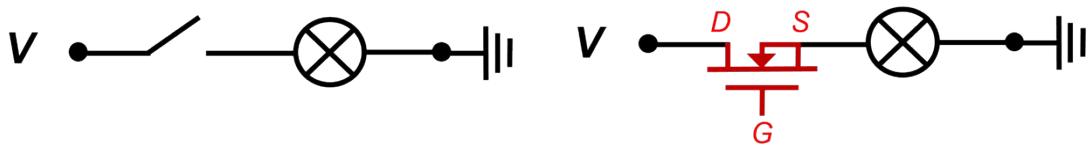

Fig. s1 Electric circuit control. (a) Electric circuit control with a hand switcher. (b) Electric circuit control with a voltage switcher, *i.e.*, metal-oxide-semiconductor field-effect transistor. When there is a positive voltage in the circuit, the circuit will automatically connect. If not, the circuit will automatically disconnect.

Table s1. Comparison of this work with state-of-art infrared regulation materials.

		A. Gorodetsky, 2018, Science (ref. 51)	*C. Kocabas, 2018, Nano Letters (ref. 52)*	*Y. Wang, 2019, Science (ref. 53)*	*J. Wu, 2021, Science (ref. 31)*	*Y. Long, 2021, Science (ref.30)*	*P. Hsu, 2023, Nature Sustainability (ref. 54)*	***This work***
Design	**Actuation**	Active	Active	Passive	Passive	Passive	Active	Passive
	Stimulation	Mechanical/ Electric	Electric	Moisture	Temperature	Temperature	Electric	Temperature
	Principle	Diffraction	hybridization	Scattering	Diffraction	Diffraction	Redox	Mixture
Performance	**Regulation range**	~0.25	0.43	>0.35	0.7	0.4	0.85	>0.52
	Regulation band	Broadband	Broadband	Broadband	Broadband	Broadband	Broadband	Selective
	Solar regulation	No	No	No	Yes	Yes	No	Yes
Feasibility	**Application**	Heating/cooling	Heating/cooling	Heating/cooling	Heating/cooling	Heating/cooling	Heating/cooling	Sub-ambient/above-ambient cooling
	Fabrication	Photolithography	Chemical vapor deposition	Photolithography	Pulse laser deposition	Spin coating	Chemical vapor deposition + photolithography	Electrospinning+ Polymerization
	Cost	High	High	High	High	Low	Very high	Low

Section 2: Design and preparation of the ISRC

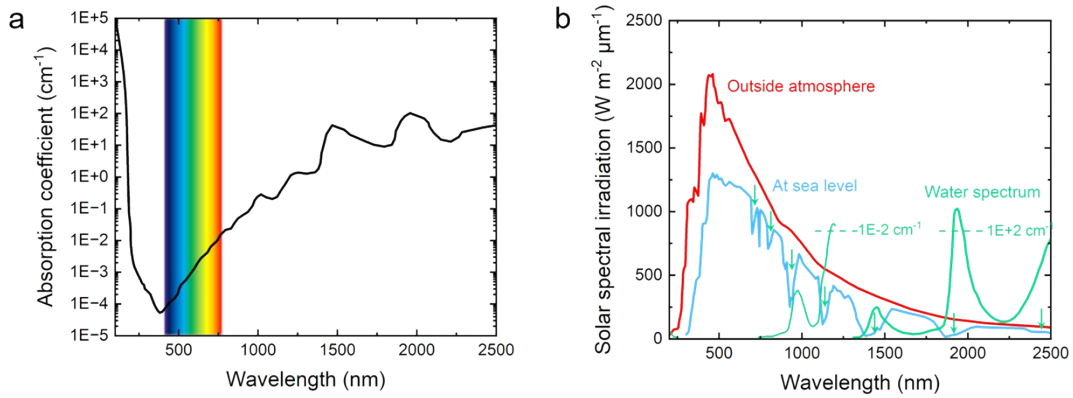

Fig. s2 Solar spectrum of atmospheric water. (a) Absorption coefficient of water in the solar region. The extremely low absorptions in the ultraviolet and visible wavelengths contribute to the transparent appearance of water. (b) Solar spectral irradiation distribution with water spectrum. The arrow shows the absorption band.

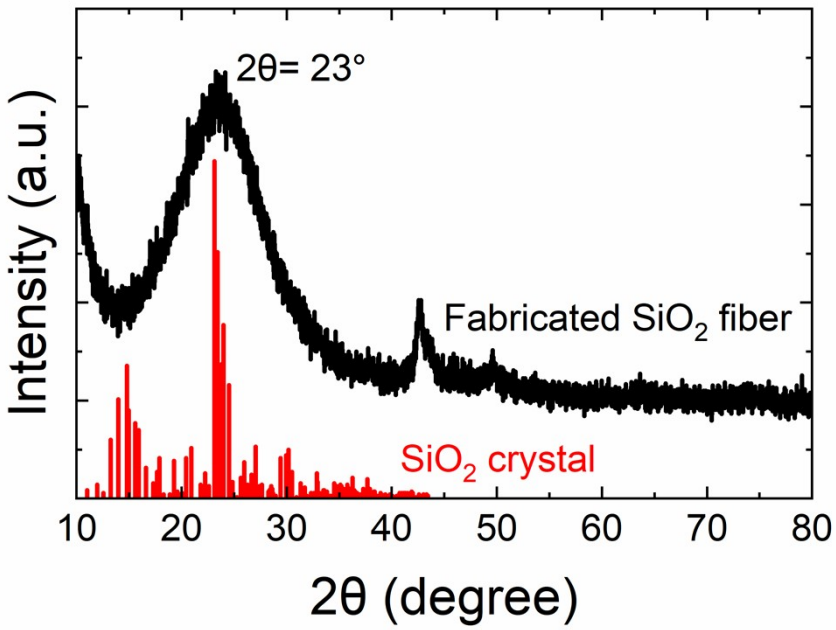

Fig. s3 XRD pattern for the fabricated SiO_2 fiber. The fabricated SiO_2 fiber shows a diffraction peak at 2θ of 23°, consistent with the stand SiO_2 crystal. The difference in diffraction patterns is due to the poor crystallinity of the prepared SiO_2. This representation well demonstrates the successful preparation of the SiO_2 fiber.

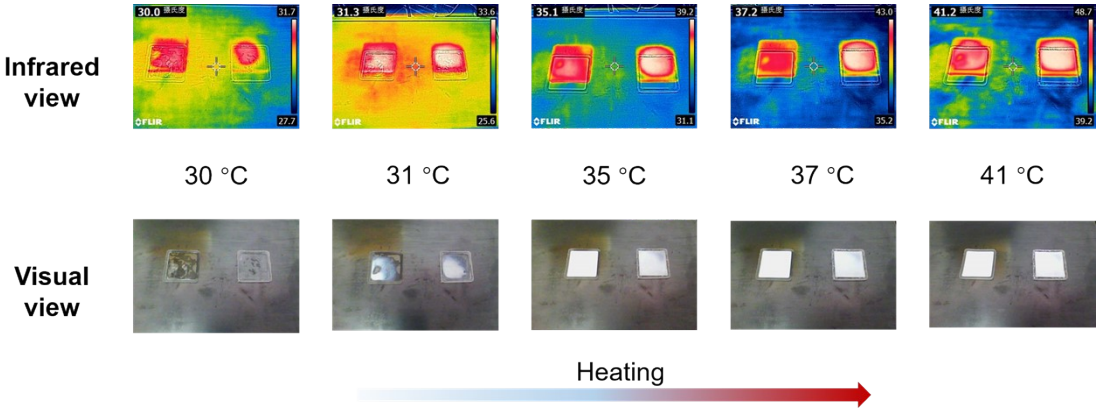

Fig. s4 Infrared and visual views of the PNIPAM hydrogels with (right)/ without (left) PE encapsulation. To verify the encapsulation effect of the PE on hydrogel, we also observed the infrared and visual views of the PNIPAM hydrogels with and without PE. It can be found that the PNIPAM with PE has a brighter infrared view (a higher temperature), indicating no significant evaporation.

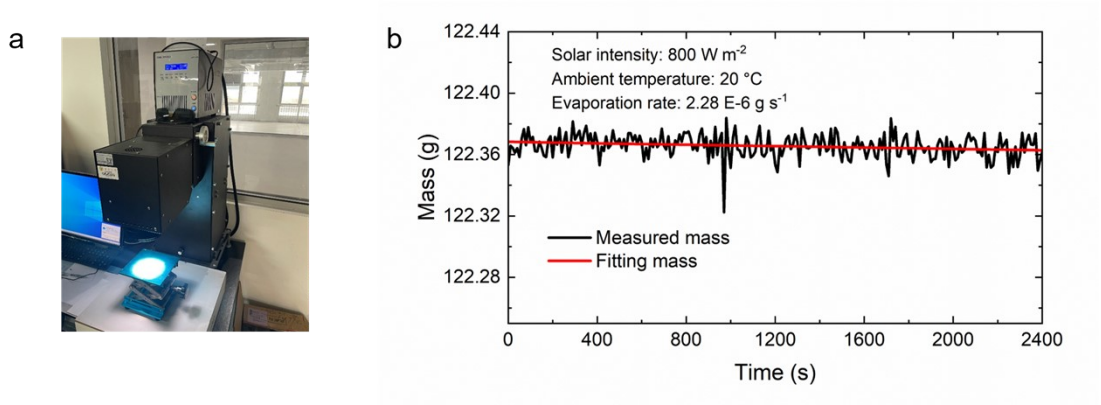

Fig. s5 Mass evolution characteristics of the ISRC under solar irradiation. (a) Photo of the solar simulator. (b) Mass curve of the ISRC. In order to verify the encapsulation effect of the PE on hydrogel, we measured the mass evolution of the ISRC with 800 Wm^{-2} solar intensity for 2400 s. It can be found that the evaporation rate is just 2.28 E-6 g s^{-1}, and the mass of the ISRC is almost unchanged. Considering the evaporation enthalpy of 2400 J g^{-1} and the ISRC area of 16 cm^2, the evaporative cooling power is just 3.42 W m^{-2}, which can be neglected.

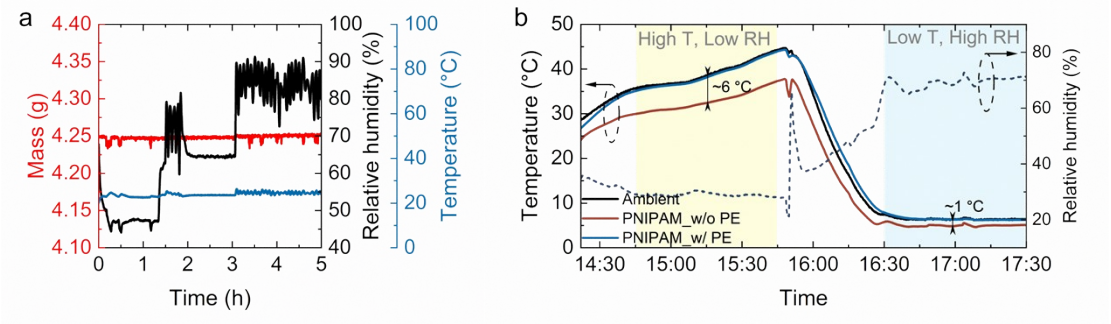

Fig. s6 Adsorption/desorption testing experiments in a temperature humidity chamber. (a) Mass evolution of the ISRC when environmental humidity changes from low to high. (b) Temperature evolution of the PNIPAM hydrogels (one encapsulated with PE, the other one without PE) in extreme environments. To examine whether vapor seeps or invades when dry or wet outside of the ISRC, we measured the mass evolution of the ISRC in a temperature humidity chamber, where the temperature was set as ~25 °C and the humidity was varying from ~45% to ~85%. As shown in Fig. s6 a, the weight of the ISRC remains unchanged during the 5-h testing, indicating its insusceptible to environmental humidity. Moreover, we measured the evaporative cooling performance of the PNIPAM hydrogel layers in high-temperature low-humidity conditions (T >35°C, RH~28%), and low-temperature high-humidity conditions (T ~5°C, RH~70%). Fig. s6 b shows that the temperature of the PNIPAM hydrogel with PE remains consistent with the ambient temperature, indicating no occurrence of evaporative cooling process. As well, the temperature of the PNIPAM hydrogel without PE shows a significant evaporative cooling temperature reduction (1~6°C). In summary, the PNIPAM hydrogel encapsulated with PE did not undergo adsorption/desorption in extreme temperature and humidity environments. In other words, the ambient humidity environment can not affect the swelling and shrinking processes of the hydrogel layer in the ISRC.

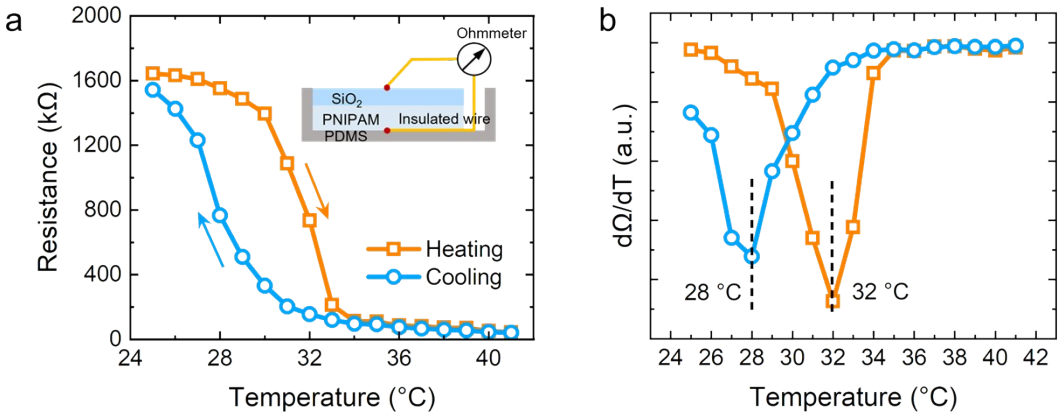

Fig. s7 Resistance change during the heating-cooling process. (a) The measured resistance. (b) The slope of resistance change. To further demonstrate the phenomenon of directional water transportation, we measured the resistance between the centers of the upper surface of the SiO_2 fiber and the bottom surface of the PNIPAM hydrogel. The little difference of the slope of resistance change in phase transform temperature is resulted from the hydrophilic property of SiO_2 fiber.

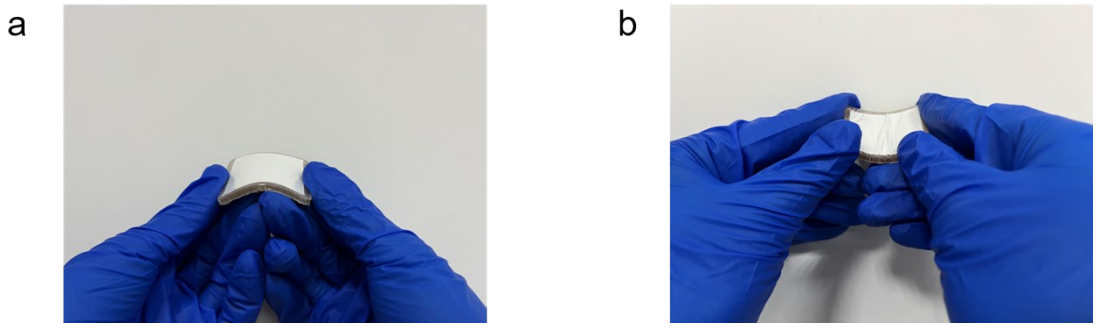

Fig. s8 Photos showing the application potential of the ISRC on curved surfaces. (a) Downward bending. (b) Upward bending. Both PNIPAM hydrogel and SiO_2 fiber have flexibility characters.

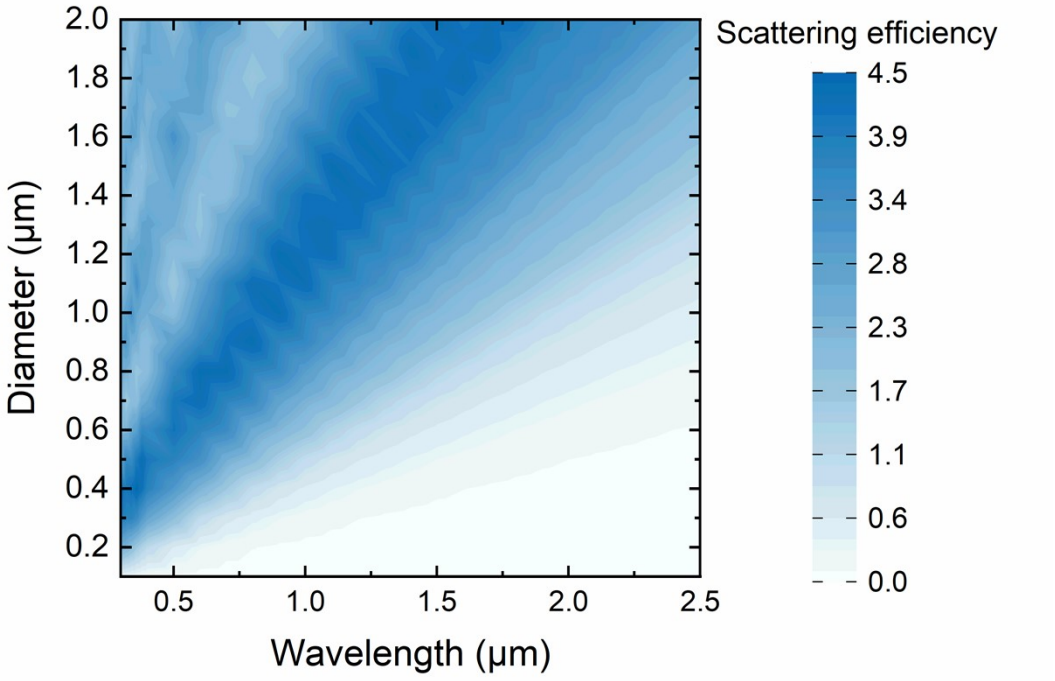

Fig. s9 Simulated scattering efficiency for SiO_2 fiber with different diameter in solar region. According to the Mie theory, the peak of the Mie scattering efficiency occurs when the size parameter approximately equals 1. So that the scattering peak broadens with the increase of diameter, meanwhile shifting to the near-infrared band. To efficiently reflect the irradiation in the whole solar region, the range where the scattering peak locates is supposed to surpass that of the solar intensity peak. Considering the solar intensity of AM 1.5, we chose the diameter range of 0.2-2.0 μm.

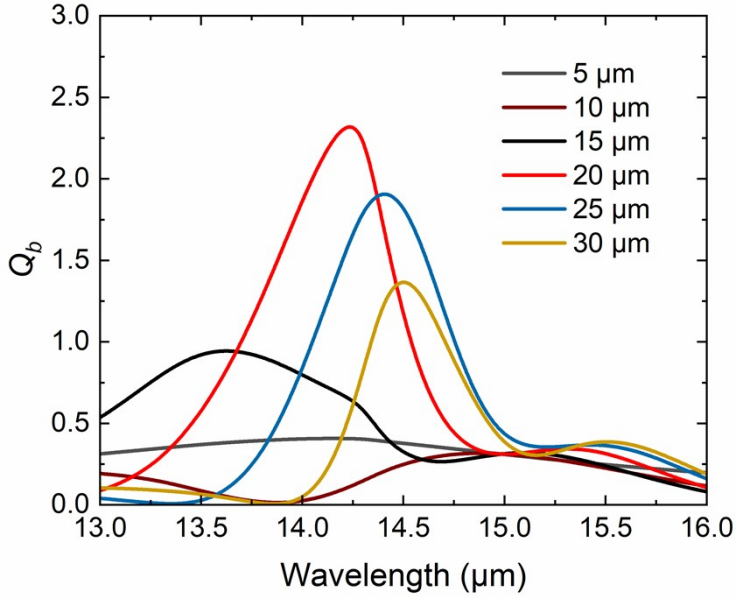

Fig. s10 Backscattering coefficient of SiO_2 particles with different diameter in the infrared region out of the atmospheric window. The original SiO_2 fiber has selective nonabsorption out of the atmospheric window. To further increase the backscattering of the incident infrared light (13-16 μm) rather than penetration, we embed the SiO_2 particle (20 μm) with highest backscattering coefficient.

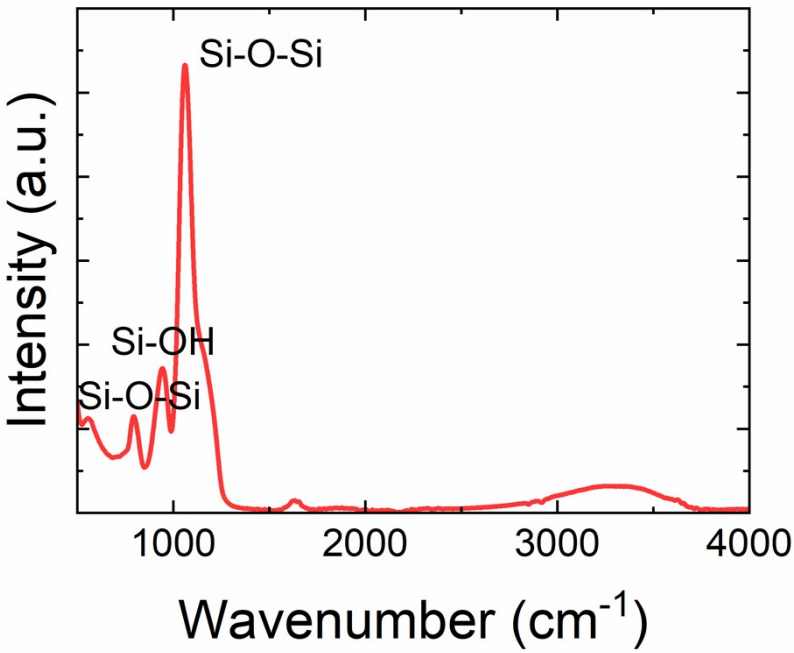

Fig. s11 ATR-FTIR curve for the fabricated SiO_2 fiber. The fabricated SiO_2 fiber shows infrared absorptions in the wavenumber of 794, 943 and 1384 cm^{-1} (*i.e.*, 12.6, 10.6, 7.22 μm), revealing a selective infrared emissivity.

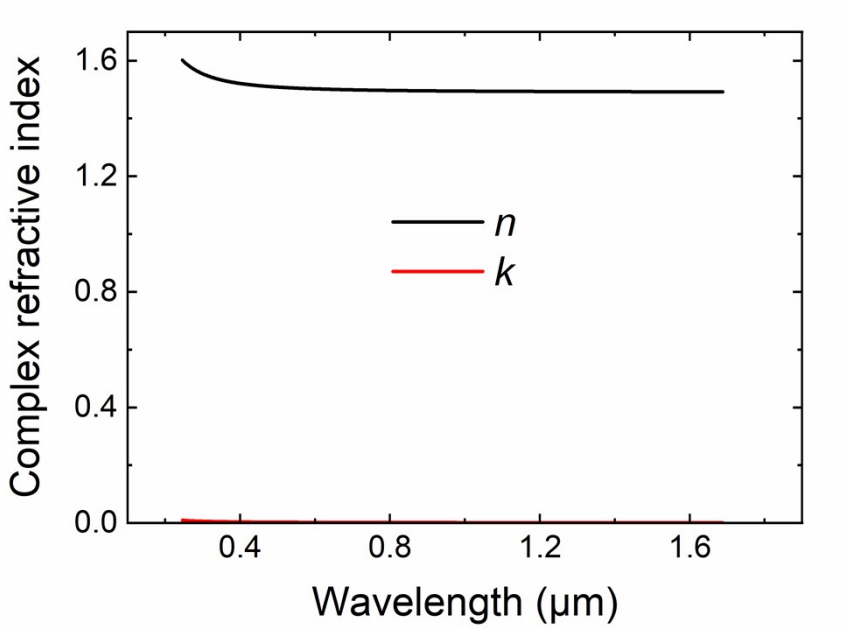

Fig. s12 Complex refractive index of PNIPAM. Herein, *n* represents refractive index, *k* represents extinction coefficient.

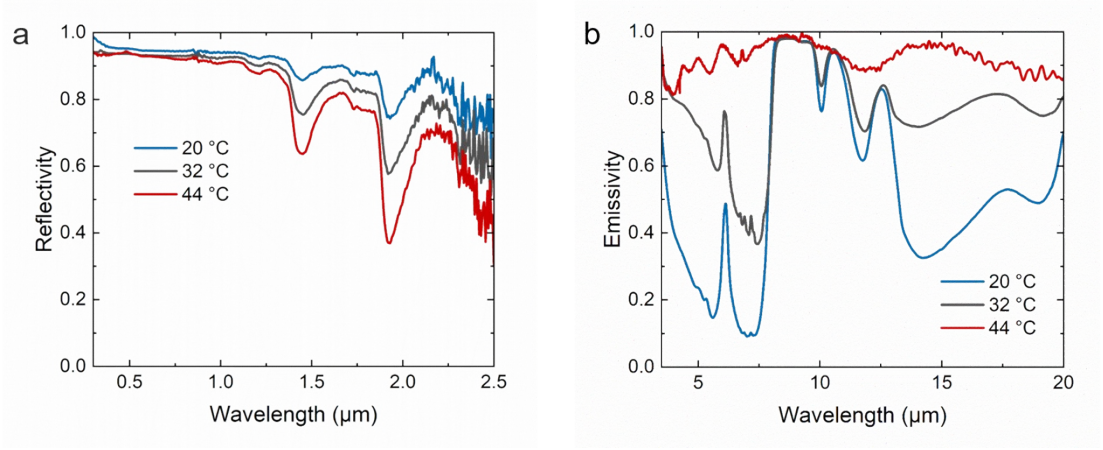

Fig. s13 Spectra evolution of the ISRC under heating. (a) Solar spectra. (b) Infrared spectra. When the temperature is below the LCST ($T_c = 20$ °C), the infrared spectrum of the ISRC reveals significant selectivity. When the temperature rises to the LCST ($T_c = 32$ °C), the infrared emissivity out of atmospheric window is greatly boosted and the solar reflectivity decreases, due to the step wetting. When the temperature surpasses the to the LCST ($T_c = 44$ °C), the infrared emissivity is further broadened and the solar reflectivity becomes stable, because of the adequate wetting.

Table s2. Standard deviations of the ISRC's reflectivity and emissivity under heating-cooling cycles

	Solar reflectivity		Infrared emissivity	
	Selective mode	**Broadband mode**	**Selective mode**	**Broadband mode**
Standard deviations	0.010	0.011	0.010	0.003

To better demonstrate the spectral stability under heating-cooling cycles, we calculated the standard deviations of the measured reflectivity and emissivity ($S = \sqrt[2]{\frac{\sum (x_i - \bar{x})^2}{N-1}}$). As shown in Table s2, the standard deviations for both reflectivity and emissivity are less than 0.011, revealing fair stability.

Section 3: Self-adaptive radiative cooling with the ISRC

3.1 Sub-ambient cooling performance of the SiO_2 fiber

Here, we firstly performed an outdoor cooling test for the single SiO_2 fiber without extra heating, to demonstrate its sub-ambient cooling performance. As shown in Fig. s14, the test was conducted on a dry and sunny day (22 August, 2023) in Yinchuan, China. The SiO_2 fiber revealed a stable cooling performance during the day, achieving an average sub-ambient temperature reduction of 4.3 °C. Even with a maximum solar irradiation of 1237 Wm^{-2}, the temperature reduction can reach 4.5 °C.

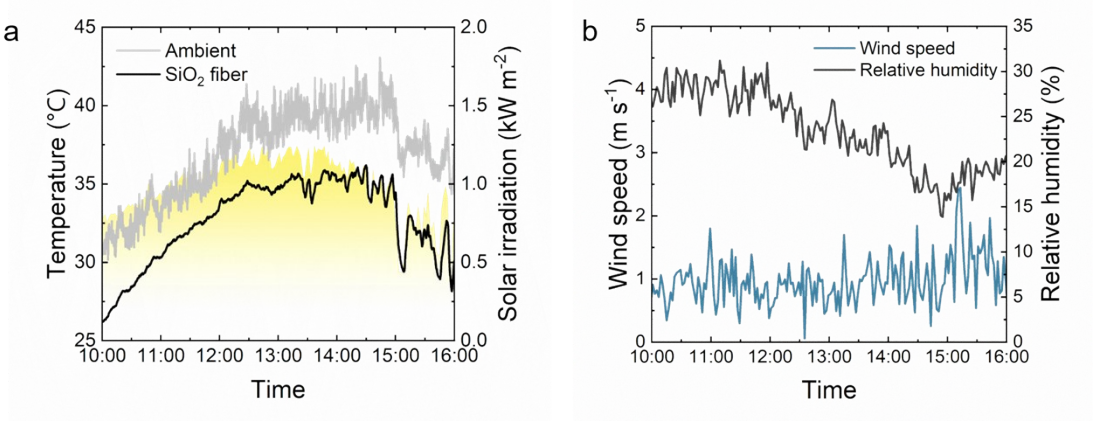

Fig. s14 Sub-ambient radiative cooling experiment with the ISRC. (a) Experimental result. (b) Weather profile.

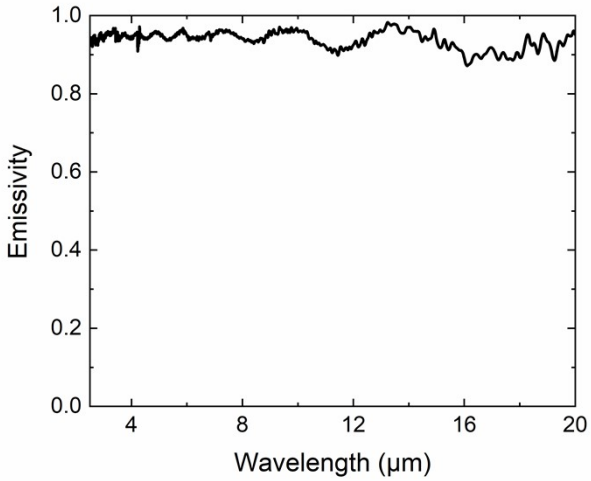

Fig. s15 IR spectrum for the black paint. The average IR emissivity is ~0.93.

3.2 Daytime sub-ambient cooling and nighttime above-ambient cooling performance of the ISRC

To comprehensively demonstrate the self-adaptive radiative cooling performance of the ISRC, we conducted daytime sub-ambient cooling and nighttime above-ambient cooling control experiments on 16 February, 2024 in Nanjing, China. As shown in Fig. s16, the daytime cooling performance of the ISRC in selective mode is similar to that of single SiO_2 fiber, realizing a sub-ambient temperature reduction of ~3.5 °C. When switched to the broadband mode with external heating (1.0 W) at night, the above-ambient cooling performance of the ISRC is on par with that of commercial black paint (broadband emitter), and the temperature is more than 6 °C lower than that of the selective SiO_2 fiber. The mass of the ISRC during heating was also measured to show that there was no significant steam overflow (Fig. s16 d).

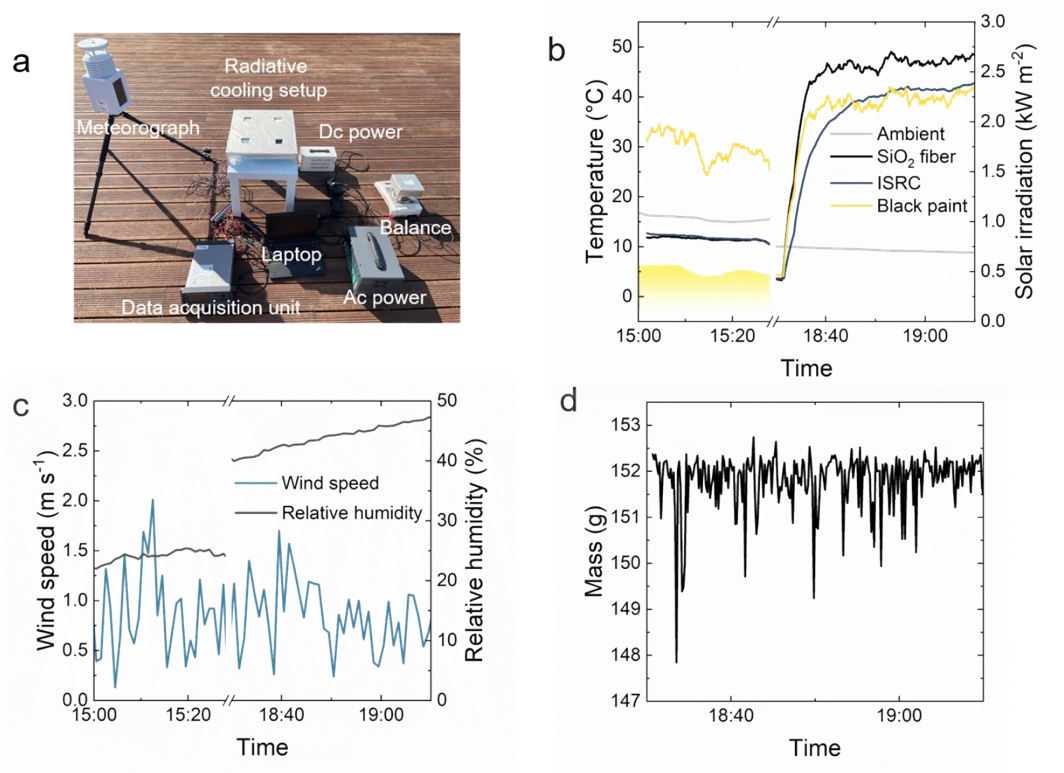

Fig. s16 Daytime sub-ambient cooling and nighttime above-ambient cooling control experiments. (a) Photo of the overall testing setups. (b) Experimental result. (c) Weather profile. (d) Mass evolution of the ISRC during nighttime above-ambient cooling experiment.

3.3 Theoretical cooling performance of the ISRC

We also calculated the theoretical cooling power of the developed ISRC and ideal coolers in above-ambient cooling conditions (Fig. s17), as well as the theoretical temperature reduction in sub-ambient cooling conditions (Fig. s18). The performance of the ISRC in broadband mode is closely aligns with ideal broadband cooler. While the performance of the ISRC in selective mode is not superior as that of the ideal selective cooler, it remains significantly better than ideal broadband cooler.

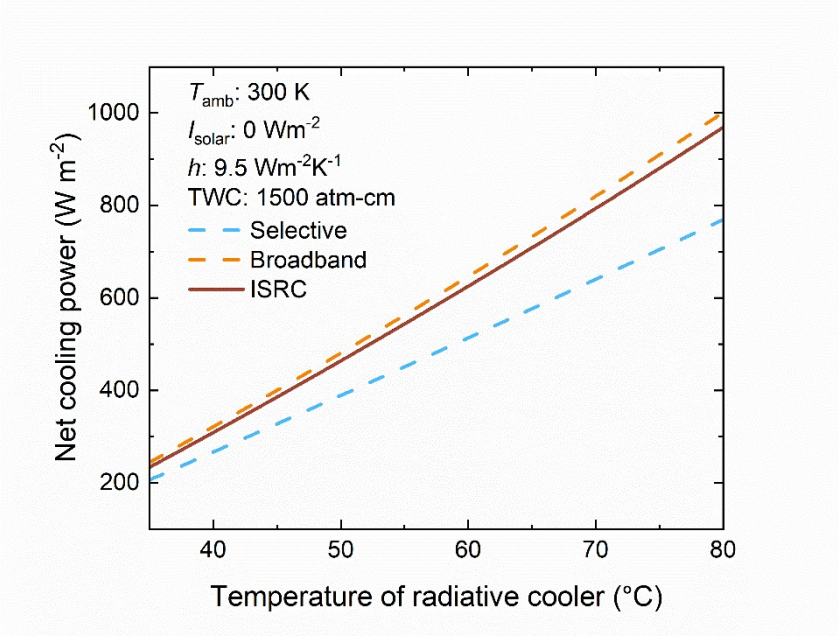

Fig. s17 Theoretical cooling power.

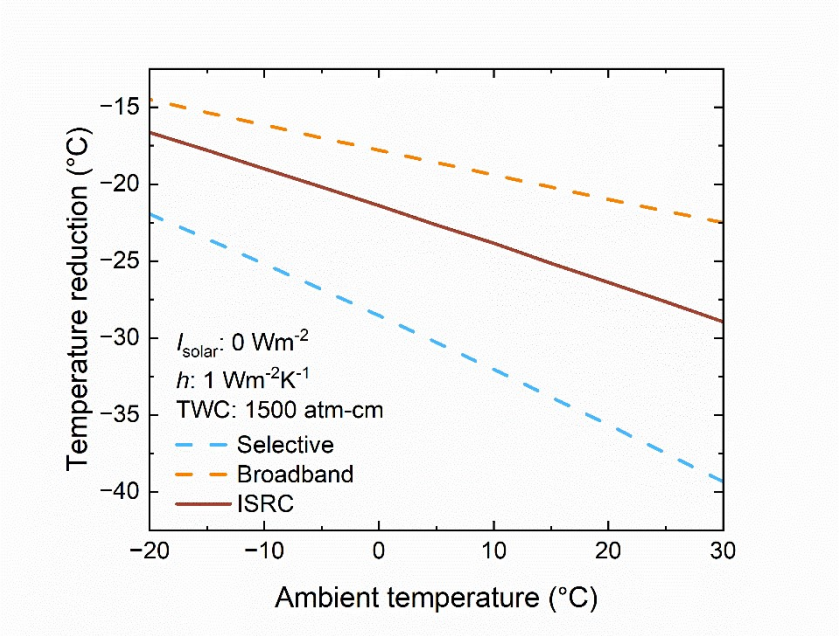

Fig. s18 Theoretical cooling temperature reduction.

Section 4: The mathematical model for the PV-TEG hybrid system

During the day, the PV cell is cooled by the cooling water produced by the ISRC. At night, the TEG directly acquires cold from the ISRC. In this way, we separately modeled the power generation processes for the PV subassembly and the TEG subassembly.

4.1 Photovoltaic generating model

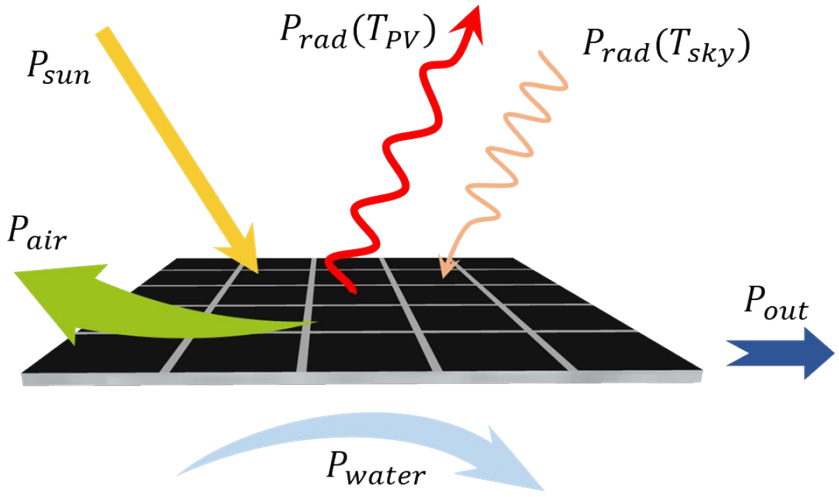

Fig. s19 Schematic of the energy flow of the PV cell.

The silicon PV cell absorbs the photons with wavelengths below 1.1 μm, leading to the generation of electron-hole pairs and the subsequent formation of electrical current. The energy balance of the PV cell can be expressed as follows:

$$P_{sun} = P_{sky} + P_{air} + P_{water} + P_{out} \tag{1}$$

In Eq (1), P_{sun} is the absorbed solar irradiation by the PV cell with an area of A, that can be defined as:

$$P_{sun} = A\int_{0.3}^{2.5} I_{sun}(\lambda)\alpha_{abs}(\lambda,\theta_{sun})cos(\theta_{sun})d\lambda \tag{2}$$

Where, $I_{sun}(\lambda)$ is the solar irradiance of AM 1.5 and θ_{sun} is the incident angle of

sunlight. $\alpha_{abs}(\lambda,\theta_{sun})$ is the spectral angular absorptivity of the PV cell in the solar region.

P_{sky} is the intrinsic radiative cooling power of the PV cell, which indicates the net emission heat to the space after counteracting the atmospheric radiation.

$$P_{sky} = P_{rad}(T_{PV}) - P_{rad}(T_{sky}) \tag{3}$$

In Eq (3), $P_{rad}(T_{PV})$ and $P_{rad}(T_{sky})$ represent the emission and absorption radiation of the PV cell, respectively.

$$P_{rad}(T_{PV}) = 2\pi A \int_0^{\frac{\pi}{2}} sin\theta cos\theta \int_{2.5}^{\infty} I_B(T_{PV},\lambda)\varepsilon_{PV}(\theta,\lambda)d\theta d\lambda \tag{4}$$

$$P_{rad}(T_{sky}) = 2\pi A \int_0^{\frac{\pi}{2}} sin\theta cos\theta \int_{2.5}^{\infty} I_B(T_{sky},\lambda)\varepsilon_{PV}(\theta,\lambda)\varepsilon_{sky}(\theta,\lambda)d\theta d\lambda \tag{5}$$

Where $I_B(T,\lambda)$ is the spectral radiation of blackbody with a temperature T at any wavelength λ by Plank's law. $\varepsilon(\theta,\lambda)$ denotes the spectral and angular emissivity of solar cells and atmosphere. According to Kirchhoff's radiation law, $\varepsilon(\theta,\lambda)$ equals to the spectral and angular absorptivity. Additionally, the spectral and angular emissivity of the atmosphere is given by:

$$\varepsilon_{sky}(\theta,\lambda) = \begin{cases} 1, for\ 3 < \lambda < 8\mu m\ or\ \lambda > 13\mu m \\ 1 - \left[1 - \bar{\varepsilon}_{sky}(0,\lambda)\right]^{1/cos\theta}, 8 \le \lambda \le 13\mu m \end{cases} \tag{6}$$

$$\bar{\varepsilon}_{sky}(0,\lambda) = 0.24 + 2.98 \times 10^{-6} P^2 exp\left(\frac{3000}{T_{sky}}\right) \tag{7}$$

Where, $\bar{\varepsilon}_{sky}(0,\lambda)$ is the atmospheric infrared transmissivity in the zenith direction in the wavelengths of 8-13 μm. P is the water vapor pressure.

P_{air} and P_{water} are the conduction and convection heat exchange on the PV cell surface with the air and the water, respectively.

$$P_{air} = Ah_{air}(T_{cell} - T_{air}) \tag{8}$$

$$P_{water} = Ah_{water}(T_{cell} - T_{water}) \tag{9}$$

Where h is the heat exchange coefficient.

$$h_{air} = 1.247(T_{cell} - T_{air})^{\frac{1}{3}} + 2.658v_{air} \tag{10}$$

$$h_{water} = \frac{\gamma Nu}{L} \tag{11}$$

In Eq (11), γ is the water thermal conductivity and L is the tube equivalent length. Nu is Nusselt number, which can be expressed as:

$$Nu = \begin{cases} 4.36, Re \leq 2320 \\ 0.023Re^{0.8}Rr^{0.4}, Re > 2320 \end{cases} \tag{12}$$

where Re and Rr are Reynolds number and Prandtl number, respectively.

P_{out} is the generated electricity power, which can be expressed as:

$$P_{out} = A\int_{0.3}^{2.5} d\lambda I_{sun}(\lambda)\alpha_{abs}(\lambda,\theta_{sun})cos(\theta_{sun})\eta(1 - \beta(T_{cell} - 298)) \tag{13}$$

β is the temperature coefficient, which is measured as -0.46%. η is the conversion coefficient of the PV cell at standard operating conditions (*i.e.*, 1000 Wm^{-2} solar irradiation and 298 K temperature), which is measured as 13.58%.

4.2 Thermoelectric generating model

Herein, we simplified the heat transfer of the TEG as a one-dimensional model, as shown in Fig. s20.

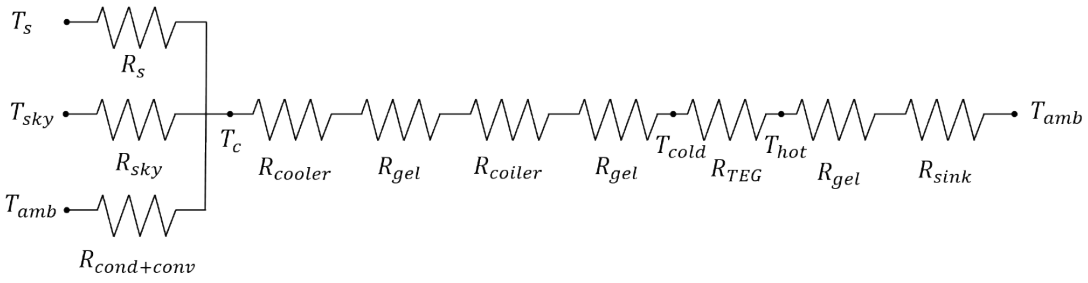

Fig. s20 Schematic of the energy flow of the TEG.

In the cold side, the TEG subassembly radiates heat to the outer space, meanwhile absorbing heat from the atmosphere (T_{sky}) and the ambient air (T_{amb}). The net cooling

power can be expressed as:

$$P_c = P_{rad}(T_c) - P_{rad}(T_{sky}) - P_{cond+conv} \quad (14)$$

In Eq (14), $P_{cond+conv}$ is the non-radiation heat exchange, which can be presented as:

$$P_{cond+conv}(T_{amb}) = Ah(T_{amb} - T_c) \quad (15)$$

Where h can be described as a function of wind speed v:

$$h = 8.3 + 2.5v \quad (16)$$

In the quasi-steady-state, the energy conservation equation of the TEG cold side can be expressed as:

$$P_c - \frac{T_c - T_{cold}}{R_{cooler} + R_{gel} + R_{coiler} + R_{gel}} = 0 \quad (17)$$

In the hot side, the TEG draws heat from the ambient air. The energy conservation equation of the TEG hot side can be expressed as:

$$P_h - \frac{T_{amb} - T_{hot}}{R_{sink} + R_{gel}} = 0 \quad (18)$$

R_{sink} is the thermal resistance of the Al heat sink, which is composed of the thermal resistance of heat sink base and fin.

$$R_{sink} = R_{base} + R_{fin} \quad (19)$$

Specifically,

$$R_{base} = \frac{L_{base}}{A_{base}k_{Al}} \quad (20)$$

$$R_{fin} = \frac{1}{\alpha_0 h_{conv} A_t} \quad (21)$$

In Eq (20), L_{base}, k_{Al} and A_{base} are the thickness, thermal conductivity and area of the heat sink base.

$$\alpha_0 = 1 - \frac{n_{fin}A_{fin}}{A_t}(1 - \alpha_{fin}) \quad (22)$$

$$\alpha_{fin} = \frac{tanh(mL_0)}{mL_0} \tag{23}$$

$$m = \sqrt{\frac{4h_{conv}}{k_{Al}D_{fin}}} \tag{24}$$

$$L_0 = L_{fin} + D_{fin}/4 \tag{25}$$

$$A_t = n_{fin}A_{fin} + A_{base} \tag{26}$$

$$A_{fin} = \pi D_{fin}L_{fin} \tag{27}$$

Where A_{fin}, D_{fin} and L_{fin} are the area, diameter and height of the heat sink fin, respectively.

The thermal power on the cold side and heat side can also be deriving from the Seebeck effect, Peltier effect, and Joule heating, as follows:

$$P_c = SIT_{cold} + \frac{T_{hot} - T_{cold}}{R_{TEG}} + \frac{1}{2}I^2R_{in} \tag{28}$$

$$P_h = SIT_{hot} + \frac{T_{hot} - T_{cold}}{R_{TEG}} - \frac{1}{2}I^2R_{in} \tag{29}$$

Where S is the Seebeck coefficient of the TEG, I is the electric current in the TEG, R_{TEG} is the thermal resistance of the TEG, and R_{in} is the electric resistance of the TEG.

In this way, the generated thermoelectric power can be expressed as:

$$P_{TEG} = P_h - P_c = SI(T_{hot} - T_{cold}) - I^2R_{in} \tag{30}$$

The generated voltage can be expressed as:

$$V_{TEG} = S(T_{hot} - T_{cold}) \tag{31}$$

When a load resistance of R_{load} is insert, the TEG power can be given by

$$P_{TEG} = \frac{[S(T_{hot} - T_{cold})]^2}{(R_{in} + R_{load})^2}R_{load} \tag{32}$$

4.3 Model validation

To validate the proposed models, the power for the PV and the voltage for the

TEG on 23 August, 2023 were iteratively calculated based on the meteorological parameters. As shown in Fig. s21 and 22, the simulated data fit well with the measured data. Meanwhile, to quantify the data deviation, we also adopted the root mean square error (RMSE) here:

$$RMSD = \sqrt{\frac{\sum_{i=1}^{n}\left(\frac{V_{sim,i} - V_{mea,i}}{V_{mea,i}}\right)^2}{n}} \tag{33}$$

The RMSE for the simulated PV power and TEG voltage are 0.034 and 0.025 respectively, accounting for extremely low differences. Such high precision of the simulations demonstrates the validity of the proposed models.

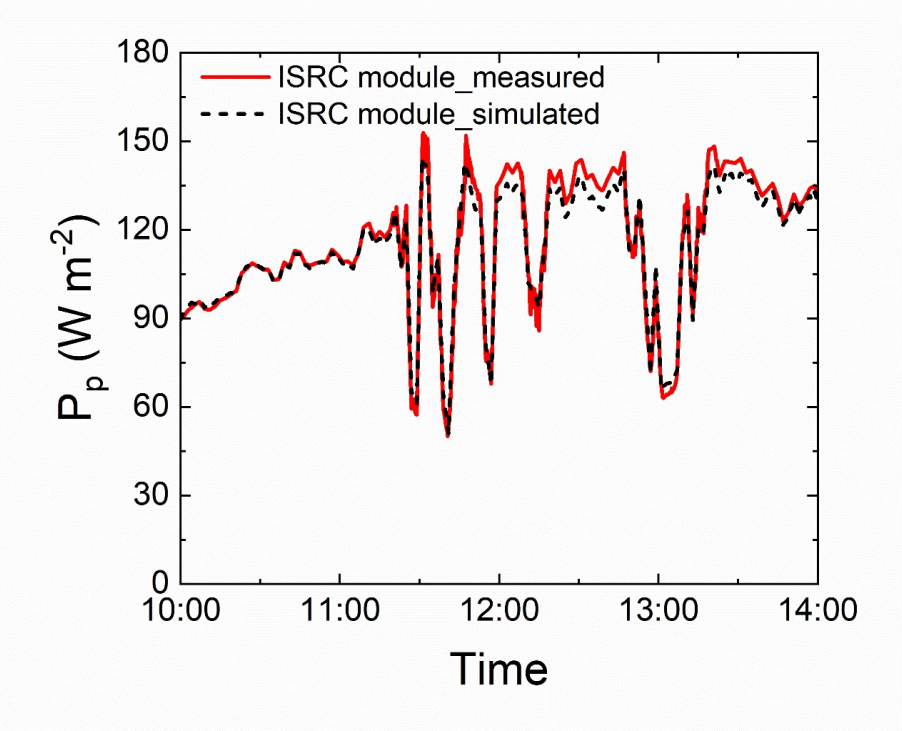

Fig. s21 Validation of the PV model.

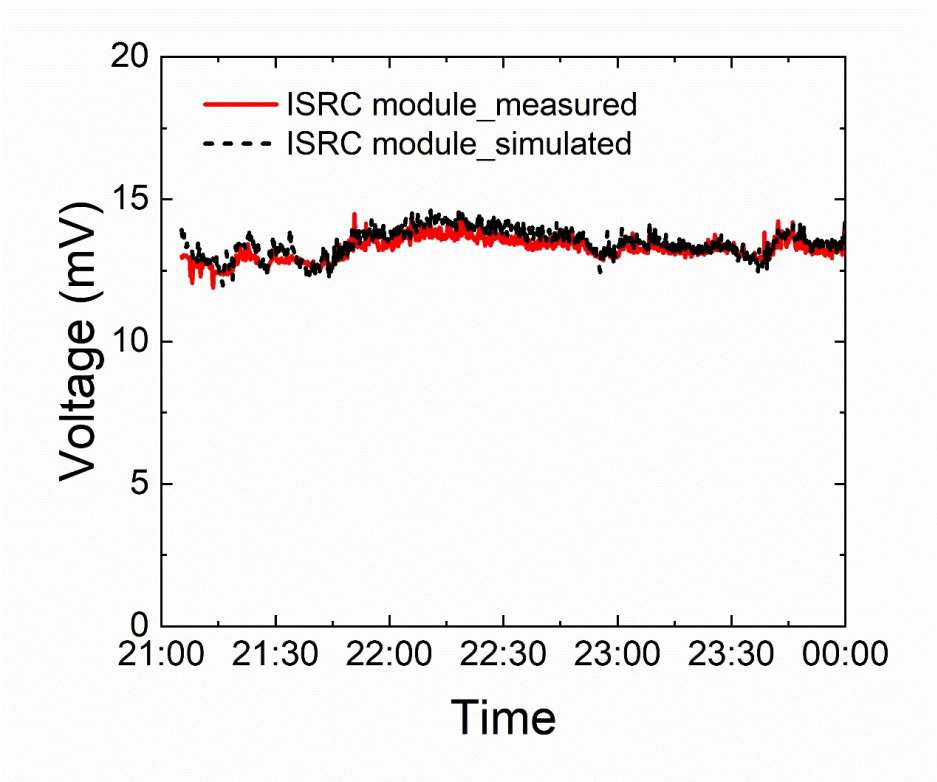

Fig. s22 Validation of the TEG model.

Section 5: Discussion for the PV-TEG hybrid system

5.1 Performance discussion

Table s3. Representative cities for Köppen-Geiger-Photovoltaic climate zones

Climate zone	AK	AH	BK	BH	CK	CH	DH	DM	DL	EM	EL	FL
Representative city	Bafata	Phitsanulok	Phoenix	Hami	Marrakech	Almeria	Atlanta	Shanghai	Berlin	Minneapolis	Moscow	Nagqu

Köppen-Geiger-Photovoltaic climate classification with the 12 most relevant climate zones (Antarctica excluded). The first letter indicates the Temperature-Precipitation (TP)-zones: A-Tropical, B-Desert, C-Steppe, D-Temperate, E-Cold and F- Polar. The second letter indicates the Irradiation (I)-zones: K-Very High, H-High, M-Medium and L-Low irradiation.

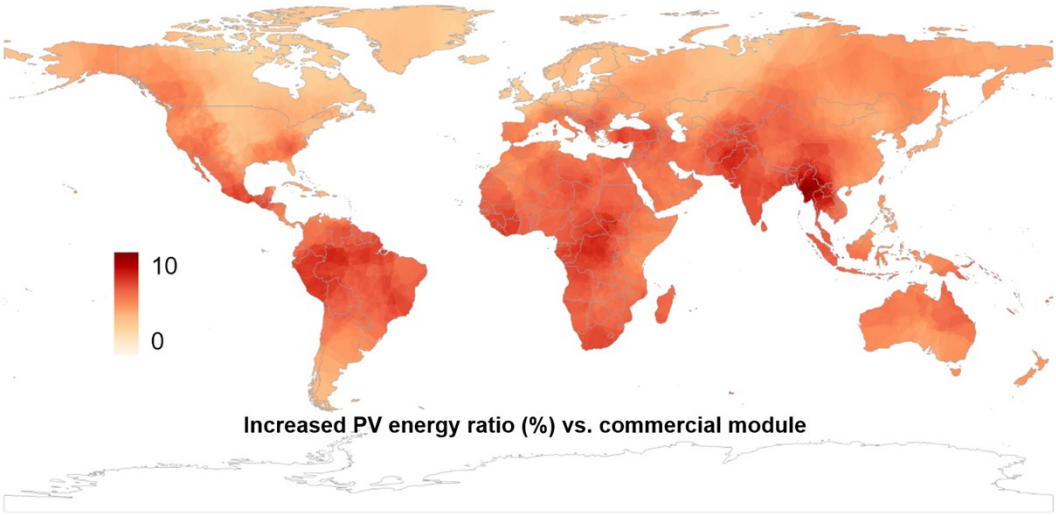

Fig. s23 Increased PV energy ratio vs. commercial module. The ISRC exhibits varying degrees of PV power generation enhancement in different regions. This map indicates that ISRC shows optimal effectiveness in specific regions, including Southeast Asia, Central Asia, Africa, and South America.

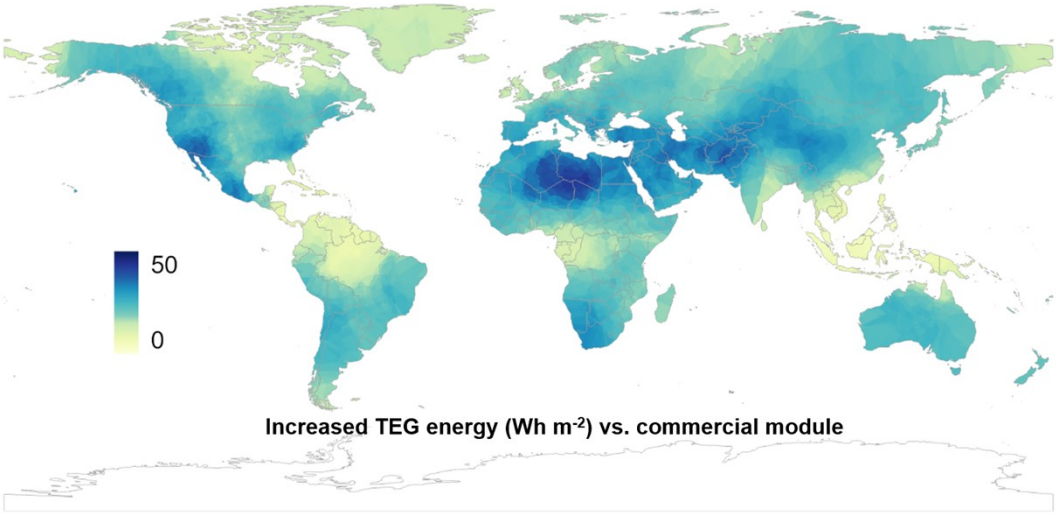

Fig. s24 Increased TEG energy vs. commercial module. The ISRC exhibits better enhancement in thermoelectric performance in the Sahara region, Central Asia, and the southern mountainous regions of the United States. This is because these areas have a drier climate and higher atmospheric window transmittance.

5.2 Economic analysis

To comprehensively evaluate the economic feasibility of the proposed PV-TEG hybrid system, we calculated the net present value (NPV) of the system, which can be expressed as:

$$NPV = \sum_{i=1}^{n} \frac{B_i - C_i}{(1+r)^i} \tag{34}$$

Where B is the present value of the benefit, C is the present value of the cost, i is the time period, r is the interest rate. The electricity price is set as 0.16 \$ kWh^{-1}.

The cost and the benefit parameters of the system are listed in Table s4. Specifically, the detailed cost for the TEG subassembly is depended on the application area (range from 0 to 100%), which should be considered from practical demand and economy. When the TEG area is equal to the RC area, the maximum cost of the TEG subassembly can reach 612 \$ m^{-2}. Meanwhile, the annual power generation is also fluctuant with scenario location.

When NPV reaches zero, the payback period can be determined. Fig. s25 shows the NPV results for the PV-TEG system with maximum power generation. It can be

found that the system exhibits fair economic feasibility, even considering 100% TEG area. While, in areas with low solar resources, the system equipped with too many TEGs for nighttime electrical generation can lead to poor economic efficiency (Fig. s26).

The specific system design should take into account the actual demand for electricity during the day and night, the local renewable energy situation, and economic conditions.

Table s4. Parameters related to economic analysis

	Cost ($ m^{-2})				**Benefit (kWh m^{-2})**
	PV subassembly	**TEG subassembly**	**RC subassembly**	**Piping subassembly**	**Annual power generation**
Proposed PV-TEG system	55.5	0-612.0	39.3	4.7	80.9-331.8

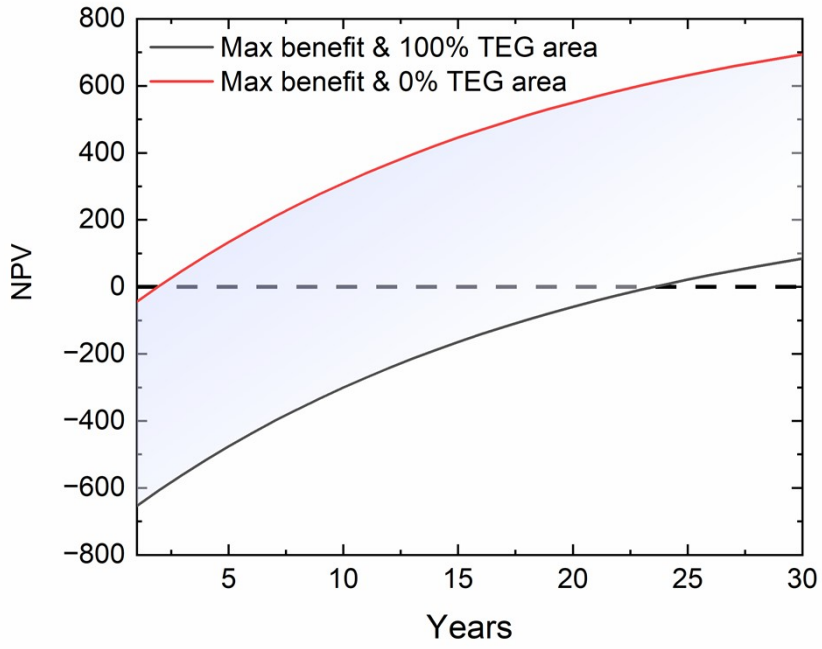

Fig. s25 The NPV results for the PV-TEG system with maximum power generation.

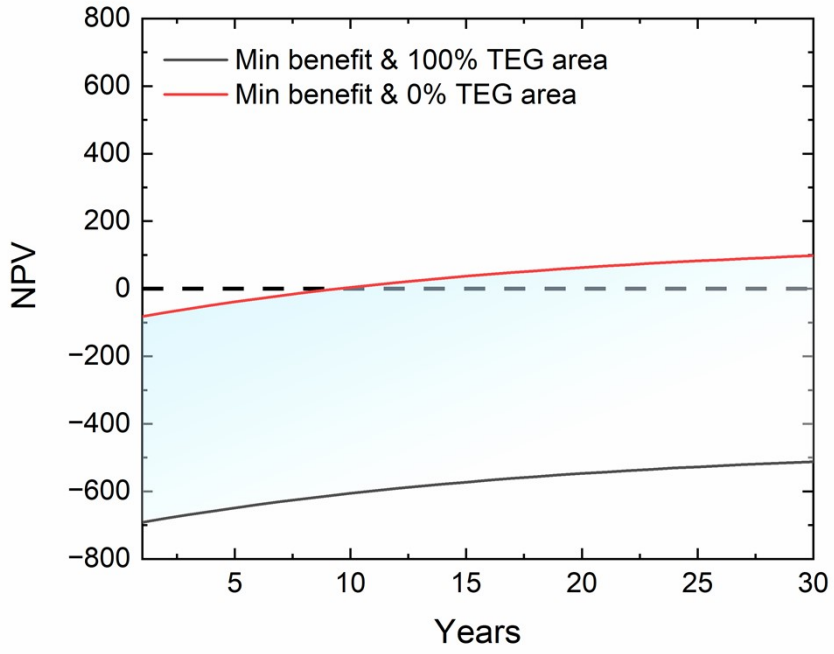

Fig. s26 The NPV results for the PV-TEG system with minimum power generation.

References

51 C. Xu, G. T. Stiubianu and A. A. Gorodetsky, *Science*, 2018, **359**, 1495–1500.

52 O. Salihoglu, H. B. Uzlu, O. Yakar, S. Aas, O. Balci, N. Kakenov, S. Balci, S. Olcum and C. Kocabas, *Nano Lett.*, 2018, **18**, 4541–4548.

53 X. A. Zhang, S. Yu, B. Xu, M. Li, Z. Peng, Y. Wang, S. Deng, X. Wu, Z. Wu, M. Ouyang and Y. H. Wang, *Science*, 2019, **363**, 619–623.

54 C. Sui, J. Pu, T. H. Chen, J. Liang, Y. T. Lai, Y. Rao, R. Wu, Y. Han, K. Wang, X. Li, V. Viswanathan and P. C. Hsu, *Nat. Sustain.*, 2023, **6**, 428–437.